C. C. Darabundit, J. S. Abel, and D. Berners, "Nyquist Band Transform:
An Order-Preserving Transform for Bandlimited Discretization"
J. Audio Eng. Soc., vol. 70, no. 9, pp. 674–689, (2022 September).
DOI: https://doi.org/10.17743/jaes.2022.0044

Nyquist Band Transform: An Order-Preserving Transform for Bandlimited Discretization

CHAMP C. DARABUNDIT, *AES Student Member*,
(champ@ccrma.stanford.edu)
JONATHAN S. ABEL, *AES Fellow* **AND DAVID BERNERS**
(abel@ccrma.stanford.edu) (dpberner@ccrma.stanford.edu)

Center for Computer Research in Music and Acoustics, Stanford University, Stanford, CA

This article proposes a method suitable for discretizing continuous-time infinite impulse response filters with features near or above the Nyquist limit. The proposed method, called the Nyquist Band Transform (NBT) utilizes conformal mapping to pre-map a prototype continuous-time system, such that, when discretized through the bilinear transform, the discretized frequency response is effectively truncated at the Nyquist limit. The discretized system shows little frequency warping when compared with the original continuous-time magnitude response. The NBT is order-preserving, parametrizable, and agnostic to the original system's design. The efficacy of the NBT is demonstrated through a virtual analog modeling application.

0 INTRODUCTION

Digital infinite impulse response (IIR) filters can be designed directly in the digital domain but are more often designed as analog filters and then discretized. The latter approach makes use of an abundance of analog filter design techniques but requires that special attention be paid to the discretization process [1–6]. Filter discretization is a particular concern in virtual analog modeling, in which it is necessary to accurately capture the behavior of unique filters or parasitic elements in audio effects [7–11].

When designing a digital filter in continuous-time, normally a Laplace transform expression is derived, and then an s-to-z mapping based on numerical integration, such as the forward or backward Euler method, is applied to derive the discretized response [12, 13]. A popular s-to-z mapping and a core focus of this article is the bilinear transform, whose standard form approximates continuous-time integration with the discrete-time trapezoidal rule. The bilinear transform has many useful properties: it is order-preserving and stability-preserving and provides a one-to-one mapping from continuous-time frequencies to discrete-time frequencies. As given by Nyquist-Shannon sampling theory, discrete-time systems are only realizable up to half the sampling rate: the Nyquist limit. As a consequence, the bilinear transform maps the infinite range of continuous-time frequencies to a finite range of discrete-time frequencies, producing frequency-warping distortion near the Nyquist limit [5, 6]. To mitigate frequency warping, a technique known as "pre-warping" utilizes a free parameter in the bilinear transform to ensure a perfect mapping from a single continuous-time frequency to a single discrete-time frequency [14]. This, however, will accentuate the effects of frequency warping away from the target pre-warping frequency.

Because pre-warping is insufficient for mitigating frequency warping near the Nyquist limit, various approaches to alleviating frequency warping have been proposed. One approach is to up-sample the filter processing, therefore artificially increasing the Nyquist limit, and then down-sample the output back to the original sampling rate [12]. This approach, however, is computationally expensive, because it requires more cycles for processing and produces latency if the resampling filter is linear phase. Said resampling filter will also affect the response near the original Nyquist limit. Another option is to use numerical optimization methods, such as least-squares, Newton's method, differential evolution, or warped Autoregressive Moving Average (ARMA) [15–19] to produce a digital response that is optimally matched to the continuous-time response below the Nyquist limit. These iterative approaches are not suitable when filter coefficients need to be computed in situ, such as in a filter with changing parameters. A separate approach is to reconstruct the desired analog system response

using Shannon's interpolation theorem, but this technique also suffers from poor resolution near the Nyquist limit [20]. Techniques that modify or utilize a different s-to-z mapping have been proposed but require careful design based on the system they are discretizing [21–23].

A separate set of methods are focused on redesigning a prototype continuous-time system in anticipation of frequency warping. When the redesigned system is discretized with a pre-warped bilinear transform, the discrete-time response will more closely match the desired prototype response. There are different techniques, each specific to the type of filters being designed, such as adjusting the quality factor (Q) in parametric filters [24–26] and shelving filters [27] or matching the asymptotic high-frequency gain at the Nyquist limit in low-pass filters [28].

Similarly, this article presents a method to produce a modified continuous-time prototype that, when discretized with the bilinear transform, is a close match to the original desired response. The proposed method, however, utilizes conformal mapping to produce a modified prototype regardless of filter type. Conformal maps are already a well-known tool in the field of filter design. The forward, backward Euler, and bilinear transform are conformal maps in the family of Möbius transforms [29, 21]. Conformal maps are utilized in warped filter design [30–32] and perceptual discretization methods such as the Bark bilinear transform [14]. Spectral transforms, such as the low-pass, high-pass, band-stop, and band-pass transforms, are conformal maps that transform the amplitude response of a filter and are named according to the effect each has on a low-pass prototype filter [33, 34].

Here, the combination of two successive transforms is leveraged to produce a *pre-mapped* continuous-time filter. The pre-mapped filter's frequency response on the entire continuous-time frequency range corresponds to the stretched response of the original prototype filter from dc to the Nyquist limit—a range denoted as *the Nyquist band*. In this way, the application of the bilinear transform produces a discretized filter with a frequency response that resembles the portion of the original continuous-time frequency response in the Nyquist band. Because the proposed method only discretizes the set of digitally realizable frequencies in the Nyquist band, this transform is named the Nyquist band transform (NBT). A comparison of frequency warping in the bilinear transform is compared to the proposed transform in Fig. 1. The frequencies warped by the bilinear transform approach infinity toward the Nyquist limit, whereas the NBT warping strays only modestly from the ideal linear characteristic.

This article is structured as follows. SEC. 1 provides background on the relationship between continuous and discrete-time domains, the bilinear transform, and spectral transforms. SEC. 2 overviews the proposed method and its constituent transforms. SEC. 3 introduces the all-pass transform, which is used to derive the component transforms. SEC. 4 derives the first transform, and SEC. 5 derives the second transform. SEC. 6 equates the geometry of the two transforms. SEC. 7 recapitulates the method and gives implementation details. SEC. 9 discusses optimization of the NBT parameter. SEC. 10 provides an example, modeling a ten-band graphic equalizer guitar pedal. SEC. 11 concludes the paper.

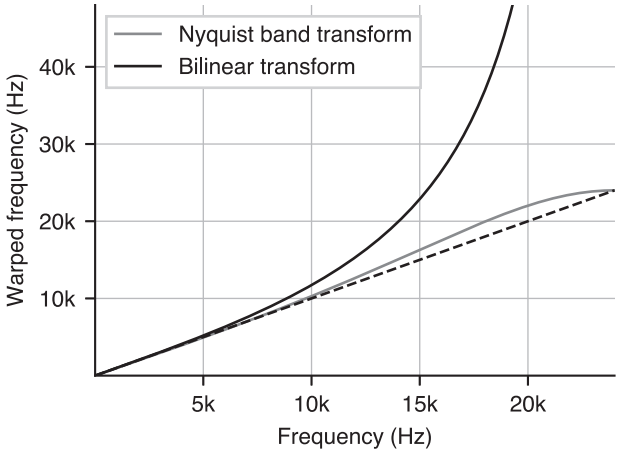

Fig. 1. Frequency warping of the proposed Nyquist band transform (gray) and bilinear transform (black) compared with the desired characteristic with no warping (dashed) for a system sampled at 44.1 kHz.

1 BACKGROUND

Before providing an overview of the method, it is necessary to first establish the relationship between the Laplace, z, and Fourier transforms and compare the continuous-time and discrete-time domains. Background on spectral transforms will then be provided.

1.1 The Continuous-Time and Discrete-Time Domains

The z-transform is analogous to a sampled version of the continuous-time Laplace transformation for a system that is assumed to be causal [35, 6, 2, 36]. The resulting relationship between the z, Laplace, and Fourier transforms and their respective variables z, s, and f is

$$z = e^{sT}, \quad s = j2\pi f = j\Omega, \quad T = \frac{1}{f_s}, \tag{1}$$

where f corresponds to frequency in hertz and f_s is the sampling rate, also in hertz, of the discrete-time system. T is the sampling period.

In this article, the following convention will be used for distinguishing frequencies in the continuous and discrete domains. For the sampling frequency f_s in hertz, the subscript is carried across:

$$\Omega_s = 2\pi f_s, \quad \omega_s = \Omega_s T, \tag{2}$$

where uppercase Ω is the continuous-time angular frequency in rads per second and lowercase ω is the discrete-time angular frequency in rads.

The domain of the Laplace transform is the complex s-plane, which will be denoted as $\mathbb{C}^S$. On the s-plane, the frequency axis corresponds to the imaginary axis and is commonly referred to as the $j\Omega$-axis. The domain of the z transform is the complex z-plane, which will be denoted

as $\mathbb{C}^Z$. On the z-plane, the frequency axis corresponds to the unit circle and is referred to as such. In the z-domain, because the frequency axis is coincident with the unit circle, frequency corresponds to angle and is bounded between values of 0 and π [6].

As a result of sampling, the stable left half of the s-plane is mapped to the interior of the unit circle in the z-plane, the unstable right half to the exterior, and the imaginary axis—in sections of $2\pi/T$—is multiply mapped to the unit circle, resulting in aliasing. The bilinear transform provides an s-plane to z-plane mapping that maps the entire $j\Omega$-axis to the unit circle.

1.2 The Bilinear Transform

A common and popular choice for s-to-z mapping is the bilinear transform. The standard forward and inverse transforms are defined as

$$g_{BT}(z^{-1}) = c\frac{1-z^{-1}}{1+z^{-1}} \quad g_{BT}^{-1}(s) = \frac{1+s/c}{1-s/c}, \quad c = \frac{2}{T}, \tag{3}$$

where c is the bilinear constant. The standard bilinear transform corresponds to the discrete-time trapezoidal rule for integration.

The bilinear transform is a specific case of a conformal map in the family of Möbius transforms and is specified by three points. The asymptotic response at infinity is mapped to π ($z = -1$), dc is mapped to digital dc ($z = 1$), and a third point is determined by c [12, 9, 29]. Using $z = e^{j\Omega T}$ in Eq. (1), the frequency warping between a continuous-time frequency Ω_a and its warped frequency Ω_d can be found by the relationship

$$\Omega_d = |g_{BT}(\Omega_a)| = c\tan\left(\frac{\Omega_a T}{2}\right), \quad c = \frac{2}{T}, \tag{4}$$

where the bilinear transform's frequency warping also corresponds to its magnitude response.

An extension of the standard bilinear transform is the *pre-warped* bilinear transform. The pre-warped bilinear transform ensures a perfect mapping at a single frequency by setting $\Omega_d = \Omega_a$ in Eq. (4) and redefining the bilinear constant.

$$c = \frac{\Omega_a}{\tan\left(\frac{\Omega_a T}{2}\right)}. \tag{5}$$

In this article, only the standard bilinear transform will be utilized.

1.3 Spectral Transforms

In the context of digital signal processing, *spectral transforms* are functions that map the frequency axis back to the frequency axis. These transforms are normally used to design low-pass, high-pass, band-pass, and band-stop filters from prototype low-pass filters [33, 34]. These transforms are conformal maps because they map lines to lines in the continuous-time domain and circles to circles in the discrete-time domain [29].

These transforms perform a change of variables and are applied through function composition. In the case of a continuous-time transfer function $H(s)$ being mapped by some continuous-time spectral transform $G(s)$, the resulting mapped transfer function $H'(s)$ is found by

$$H'(s) = (H \circ G)(s) = H\left(G(s)\right). \tag{6}$$

The change of variables is found through evaluation of the transform function. If $G(j\Omega_2) = j\Omega_1$, composing $H(s)$ with $G(s)$ results in the behavior of $H(s)$ at Ω_1 being mapped to Ω_2 in $H'(s)$. More succinctly,

$$H'(j\Omega_2) = H\left(G(j\Omega_2) = j\Omega_1\right) = H(j\Omega_1). \tag{7}$$

By the definition of a spectral transform, a continuous-time transform must have a phase response equal to either $\pm 90^\circ$ because the transform maps only to the $j\Omega$-axis. In discrete-time, a spectral transform must have a constant amplitude response equal to unity because the transform can map only to the unit circle. As such, the frequency warping of a continuous-time spectral transform—with real coefficient transforms and a Hermitian frequency response—can be evaluated through the amplitude response of the transform. The frequency warping of a discrete-time spectral transform can be evaluated through the phase response of the transform.

The bilinear transform can be thought of as a special case of a spectral transform, in the sense that it maps the frequency axis back to itself. However, the bilinear transform maps the continuous-time frequency axis to the discrete-time frequency axis.

2 OVERVIEW OF THE METHOD

The authors begin with a prototype continuous-time system that they wish to discretize with the standard bilinear transform. First, it is important to recognize that the bilinear transform maps the entire $j\Omega$-axis in the complex s-plane to the unit circle in the z-plane, and the effective frequency mapping in hertz is

$$[0, \infty) \in \mathbb{C}^S \rightarrow [0, f_s/2) \in \mathbb{C}^Z. \tag{8}$$

The above states the bilinear transform compresses an infinite set of frequencies from $[0, \infty)$ in the continuous-time domain to a set of frequencies from $[0, f_s/2)$ in the discrete-time domain. A result of this compression is the frequency warping described by Eq. (4). To address the frequency warping caused by the bilinear transform, a series of continuous-time transforms is used to pre-map the prototype system such that the finite Nyquist band is stretched over the entire continuous-time frequency axis.

The first transform in the proposed method is a second-order continuous-time transform designed to have a critical point at the Nyquist limit. As a result of this critical point, the Nyquist band is mapped twice to the $j\Omega$-axis. The mapping in hertz is

$$[0, f_s/2) \in \mathbb{C}^S \rightarrow [0, f_s/2), (\infty, f_s/2) \in \mathbb{C}^S. \tag{9}$$

The Nyquist band $[0, f_s/2)$ is mapped back to Nyquist band $[0, f_s/2)$ in addition to being flipped and stretched across the range from the Nyquist limit to infinity. The order of ∞ and $f_s/2$ within the second set in Eq. (9) is flipped to represent

that dc is mapped to infinity and the Nyquist limit back to itself.

The second transform in the proposed method is the inverse of a transform similar to the first transform. The similar transform, which is denoted the forward second transform, likewise has a critical point at the Nyquist limit. However, instead of mapping a segment of the frequency axis, the forward second transform will map the entire $j\Omega$-axis back to the $j\Omega$-axis twice. The inverse second transform reverses the forward mapping, and the effective mapping in hertz is thus

$$[0,\ f_s/2), (\infty,\ f_s/2) \in \mathbb{C}^S \rightarrow [0,\ \infty) \in \mathbb{C}^S. \tag{10}$$

Here, two bands from $(0,\ f_s/2)$ and $(\infty,\ f_s/2)$ are mapped back to the entire $j\Omega$-axis.

Because the second transform is not the inverse of the first transform, a pole and zero stabilization step is necessary so that the inverse second transform can be applied to the first transform.

After stabilizing the poles and zeros, the inverse second transform can be applied to the system mapped by the first transform. The original response has now been pre-mapped such that the Nyquist band is stretched across the entire continuous-time frequency axis.

$$[0,\ f_s/2) \in \mathbb{C}^S \rightarrow [0,\ \infty) \in \mathbb{C}^S. \tag{11}$$

When this stretched response is discretized with the bilinear transform, the effective frequency mapping ideally maps the Nyquist band in continuous-time to the Nyquist band in discrete-time.

$$[0,\ f_s/2) \in \mathbb{C}^S \rightarrow [0,\ f_s/2) \in \mathbb{C}^Z. \tag{12}$$

The steps of the NBT process are illustrated in the diagram in Fig. 2. The process of the NBT is also shown applied to a fourth-order low-pass Chebyshev filter in Fig. 6. The two transforms used in the proposed method will be derived using the form of the discrete-time all-pass transform.

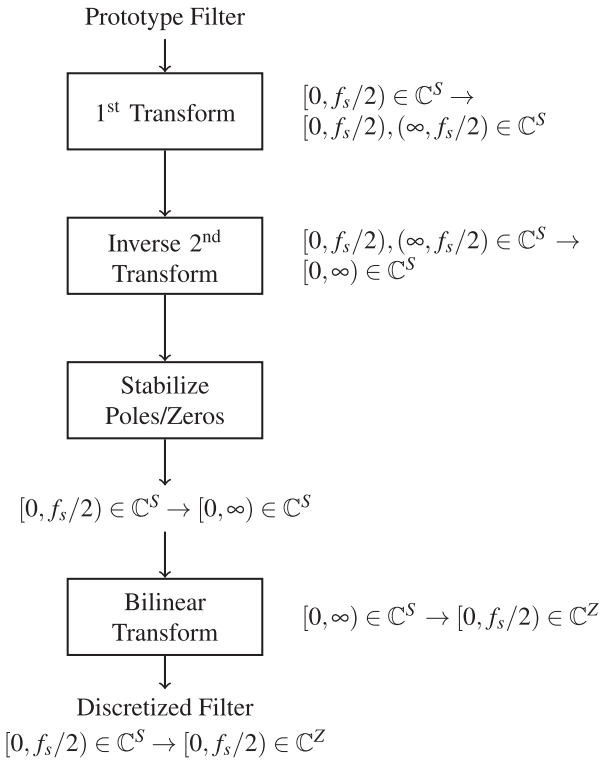

Fig. 2. Nyquist band transform process. The individual steps of the process are shown on the left, starting with a prototype filter. On the right are the effective frequency mappings in hertz at various stages of the process.

3 THE ALL-PASS TRANSFORM

Although the proposed method utilizes continuous-time spectral transforms, in practice, it is easier to derive the required spectral transform in the discrete-time domain using the form of the all-pass transform. The all-pass transform is a z-domain spectral transform that has been widely used in audio signal processing for warping the frequency axis in the discrete-time domain [37, 30, 19, 32, 14]. The all-pass transform shares its definition with the all-pass filter because the unity amplitude response is the criteria for a discrete-time spectral transform.

$$g(z^{-1}) = e^{j\theta} \prod_{i=1}^{n} \frac{p_i - z^{-1}}{1 - p_i z^{-1}} \tag{13}$$

Here, n is the order of the transform, and p_i is the pole location of each cascaded first-order all-pass section. Lowercase $g(\cdot)$ is used to distinguish discrete-time and continuous-time transforms. The order of a spectral transform increases the order of a mapped system by a factor of the spectral transform's order. A second-order all-pass transform would double the order of the system it is applied to.

The all-pass transform provides a practical framework for deriving spectral transforms because it is only parameterized by the location of its poles. Additionally, enforcing the all-pass criteria is more straightforward than enforcing the $\pm 90^\circ$ phase response criteria for continuous-time spectral transforms.

The all-pass transform manipulates the frequency axis through warping angle, which corresponds to frequency in the z-domain. Mappings can be determined by evaluating the phase response of the transform.

The continuous-time equivalent spectral transform can be derived by first composing the standard bilinear transform with the discrete-time all-pass transform and then composing the result with the inverse bilinear transform.

$$G(s) = \left[(g_{BT} \circ g) \circ g_{BT}^{-1}\right](s) \tag{14}$$

Because the bilinear transform maps the entire continuous-time frequency axis to the entire discrete-time frequency axis, using the forward and inverse bilinear transform as such ensures that the continuous-time transform $G(s)$ that results from Eq. (14) is a spectral transform. The series mapping in Eq. (14) can be used to determine continuous-time equivalents of common discrete-time spectral transforms as shown in Table 4.

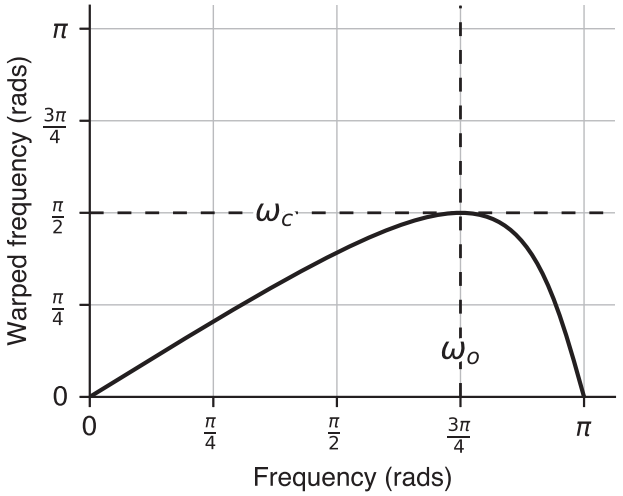

Fig. 3. Frequency warping of the discrete-time all-pass first transform from Eq. (23). The transform maps dc to both dc and π (the Nyquist limit). The truncation frequency $\omega_c = \frac{\pi}{2}$ is mapped to the critical frequency $\omega_o = \frac{3\pi}{4}$.

4 DERIVATION OF THE FIRST TRANSFORM

The first transform will now be derived. For the first transform, the authors are seeking the effective mapping in Eq. (9) and illustrated in Fig. 3. The authors are looking to map a truncated segment of the frequency axis, from dc to some frequency ω_c, back to the frequency axis twice about a critical frequency ω_o. The effective mapping that needs to be derived in discrete-time is

$$[0, \omega_c] \in \mathbb{C}^Z \rightarrow [0, \omega_o), (\omega_o, \pi) \in \mathbb{C}^Z, \tag{15}$$

where ω_c is the truncation frequency and ω_o is the critical frequency.

First, a cascade of two first-order all-pass sections with possibly complex poles p_1 and p_2 is defined.

$$g(z^{-1}) = \frac{p_1 - z^{-1}}{1 - p_1 z^{-1}} \frac{p_2 - z^{-1}}{1 - p_2 z^{-1}}. \tag{16}$$

This transform must have real coefficients such that the resulting mapped system to also have real coefficients. If p_1 and p_2 are complex, they must be complex conjugates ($p_1 = p_2^*$) for the transform to have real coefficients.

As shown in Fig. 3 and stated in Eq. (15), the transform maps dc to both dc and π, the Nyquist limit, and ω_c to ω_o. At the critical frequency ω_o, the transform reaches its warped frequency maxima ω_c. Thus, group delay of the transform at the critical angle ω_o must be $-\frac{d}{d\omega}\Theta(\omega_o) = 0$, where $\Theta(\omega)$ is the phase response of the transform. The group delay of the transform is

$$-T\left[\frac{p_1^2 - 1}{p_1^2 - 2p_1\cos(\omega_o) + 1} + \frac{p_2^2 - 1}{p_2^2 - 2p_2\cos(\omega_o) + 1}\right] = 0. \tag{17}$$

Solving for p_1 in terms of p_2,

$$p_1 = \frac{p_2\cos(\omega_o) - 1}{p_2 - \cos(\omega_o)} \quad \text{or} \quad \frac{1}{p_2}. \tag{18}$$

The authors choose the former solution because the latter solution represents the trivial case in which the all-pass transform is equal to unity. If p_2 is assumed to be stable ($|p_2| < 1$), because cosine is bounded between $[-1, 1]$, the solution to p_1 in Eq. (18) will necessarily appear outside the unit circle, and $p_1 \neq p_2^*$. For real-valued coefficients, p_1 and p_2 must also be real-valued. Consequently, if p_1 is unstable, then the transform is unstable, and any filter mapped by the transform will be unstable as well.

The solution to p_1 is then simplified by arbitrarily setting the critical frequency $\omega_o = \pi/2$. The relationship between the poles in Eq. (18) reduces to

$$p_1 = -\frac{1}{p_2}. \tag{19}$$

By substituting Eq. (19) into Eq. (16), dropping the subscripts, and mapping the truncation frequency ω_c to $\pi/2$,

$$e^{-j\omega_c} = g(e^{-j\pi/2}) = \frac{p - j(p^2 - 1) + p}{-p - j(p^2 - 1) - p}. \tag{20}$$

The pole location p is solved, and the following is found:

$$p = \tan\left(\frac{\omega_c}{4}\right) \quad \text{or} \quad -\frac{1}{\tan\left(\frac{\omega_c}{4}\right)}. \tag{21}$$

The two solutions restate the relationship between the poles in Eq. (19) and either is valid. The critical frequency parameter $\omega_o = \pi/2$ is then allowed to be mapped to any angle $\hat{\omega}_o$ by composing the result in Eq. (21) with a first-order, low-pass, all-pass transform defined by [37].

$$g_{LP}(z^{-1}) = \frac{a + z^{-1}}{1 + az^{-1}},\ a = \tan\left(\frac{1}{2}\left(\hat{\omega}_o T - \frac{\pi}{2}\right)\right). \tag{22}$$

The resulting discrete-time transform with critical frequency $\omega_o = \hat{\omega}_o$ and truncation frequency ω_c is then

$$g_1(z^{-1} = (g \circ g_{LP})(z^{-1}) = \frac{z^{-2} + \alpha_1 z^{-1} + \alpha_0}{\alpha_0 z^{-2} + \alpha_1 z^{-1} + 1}, \tag{23}$$

where

$$\alpha_1 = -\frac{2\cos\left(\frac{\omega_c}{2}\right)}{\cos\left(\frac{2\omega_o + \omega_c}{2}\right)}, \tag{24}$$

$$\alpha_0 = \frac{\cos\left(\frac{2\omega_o - \omega_c}{2}\right)}{\cos\left(\frac{2\omega_o + \omega_c}{2}\right)}. \tag{25}$$

A frequency warping produced by Eq. (23) is shown in Fig. 3. Using Eq. (14), the continuous-time equivalent transform of Eq. (23) is

$$G_1(s) = -\frac{2\Omega_o\Omega_c s}{s^2 - \Omega_o^2}, \tag{26}$$

where ω_o and Ω_o are the critical frequencies and ω_c and Ω_c are the truncation frequencies in discrete-time and continuous-time transforms, respectively. For $s = j\Omega_o$ and $\Omega_c = \Omega_o$, the function maps Ω_o to Ω_o. Because the transform is unstable, any filter created using the derived transform must be stabilized. In the z-plane, this is done by taking the reciprocal of any poles outside the unit circle or,

in the s-plane, by reflecting any poles in the right-half plane across the imaginary axis to the left-half plane.

5 DERIVATION OF THE INVERSE SECOND TRANSFORM

The second transform performs a similar but inverse mapping of the first transform. To derive the inverse second transform, the forward second transform will first be derived, and its free parameter γ will be discussed. The matrix representation of spectral transforms is then utilized to derive a numerical representation of the inverse second transform. This numerical representation avoids a fractional-order inverse transform and thus a fractional-order mapped filter.

5.1 The Forward Second Transform

The effective mapping of the forward second transform in hertz is

$$[0, \infty) \in \mathbb{C}^S \rightarrow [0, f_o), (\infty, f_o) \in \mathbb{C}^S, \tag{27}$$

where f_o is once again the critical frequency of the transform. This mapping is the same as the band-stop, also called band-elimination, transform. To derive the continuous-time transform, Eq. (14) is applied to the solution in [33].

For the forward second transform, the numerator parameters in Table 4 will be replaced with a single lumped parameter γ, and the forward second transform is

$$G_2(s) = \frac{\gamma s}{s^2 + \Omega_o^2}. \tag{28}$$

When $s = j\Omega_o$, the transform approaches infinity. Thus, the asymptotic behavior at infinity is mapped to the radian frequency Ω_o. For $\Omega < \Omega_o$, the frequency range between dc to infinity is mapped between dc and f_o, and for $\Omega > \Omega_o$, the mapped frequencies are inverted about Ω_o. This corresponds to the desired mapping in Eq. (27).

The frequency mapping below f_o, in which an infinite frequency range is compressed to a finite frequency range, draws similarity to the bilinear transform. Fig. 4 demonstrates the similarity of these two transforms when $\Omega_o = \pi f_s$, $\gamma = \Omega_o^2$, and $f_s = 40$ kHz.

The parameter γ scales the mapped frequencies. The numerator parameters in Table 4 are simplified because the authors wish to parameterize the forward transform based on the successive frequency warpings in the proposed Nyquist band transform.

5.2 Determining γ

γ represents a free parameter and can be used to ensure a perfect mapping of a single frequency throughout the proposed discretization process. Doing so involves accounting for the frequency warping produced by the first transform, inverse second transform, and standard bilinear transform.

First, consider the frequency warping caused by the first transform. How a frequency of interest Ω_a is mapped by the first transform to a new frequency Ω_1 can be derived by evaluating

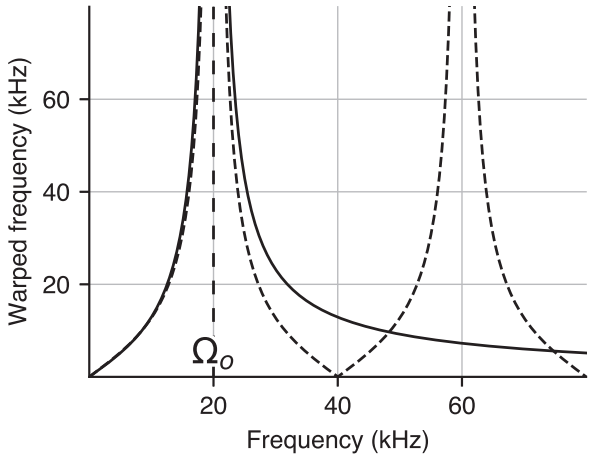

Fig. 4. Comparison between frequency warping of the bilinear transform and forward second transform in Eq. (28) with $f_s = 40$ kHz. The original frequency on the y-axis is mapped multiply to frequencies on the x-axis in intervals of $n\frac{f_s}{2}$, $n = 1, 2, \cdots$ in the case of the bilinear transform and twice in the case of the second forward transform. The frequency warping between the two transforms is similar below $\Omega_o \propto f_s/2$

$$\Omega_a = |G_1(j\Omega_1)|. \tag{29}$$

Because $G_1(\cdot)$ is a second-order transform, determining Ω_1 results in a quadratic. The lesser solution to this quadratic is chosen because this corresponds to the lower band of the first transform. This will map positive frequencies back to the positive frequency axis. The frequency warping between Ω_1 and Ω_a is

$$\Omega_1 = \frac{\Omega_o}{\Omega_a}\left(\Omega_c - \sqrt{\Omega_c^2 - \Omega_a^2}\right). \tag{30}$$

Now, to compute where Ω_a is warped by the inverse second transform, evaluate

$$\Omega_2 = |G_2(j\Omega_1)|. \tag{31}$$

Notice that evaluating the mapping from Ω_2 to Ω_1 in the forward second transform is equivalent to evaluating the mapping from Ω_1 to Ω_2 for the inverse second transform. The expression in Eq. (31) can be solved for γ by substituting in Eq. (30)

$$\gamma = 2\Omega_o \frac{\Omega_2}{\Omega_a}\sqrt{\Omega_c^2 - \Omega_a^2}. \tag{32}$$

Finally, to account for the frequency warping in the standard bilinear transform, Eq. (4) is utilized, and Ω_2 is mapped back to Ω_a, which gives

$$\Omega_2 = \frac{2}{T}\tan\left(\frac{\Omega_a T}{2}\right). \tag{33}$$

A value of γ accounting for frequency warping throughout the entire discretization process is then

$$\gamma = 2\Omega_o \frac{\frac{2}{T}\tan\left(\frac{\Omega_a T}{2}\right)}{\Omega_a}\sqrt{\Omega_c^2 - \Omega_a^2}. \tag{34}$$

With $\Omega_o = \Omega_c = \pi f_s$, γ is be parameterized by the sampling rate and a frequency of interest Ω_a. γ determines an additional point of intersection, outside of dc and the Nyquist limit, with the linear frequency mapping. If there is no a priori of the system, a possible choice for γ is to set $\Omega_a = \pi f_s/4$: half the Nyquist limit. This results in a $\gamma = 4\sqrt{3}\pi f_s^2 \approx 2.2\Omega_o^2$. Improvements to this value can be made through optimization as in SEC. 9. To invert the forward second transform, matrix representation of spectral transforms is utilized to numerically represent the inverse second transform.

5.3 Matrix Representation of Spectral Transforms

To apply a spectral transform to an IIR filter, rather than use function composition, the transform is represented as a matrix transformation that maps the original filter coefficients to a new set of mapped coefficients [38].

A general continuous-time IIR transfer function is defined as

$$H(s) = \frac{(0)s^N + (0)s^{N-1} \cdots + b_M s^M + \cdots + b_0}{a_N s^N + a_{N-1}s^{N-1} \cdots + a_0}, \quad (35)$$

where M and N are the order of the numerator and denominator polynomials, with $N \geq M$. If $N < M$, the system simplifies to a finite impulse response term combined with an IIR term. A similar matrix method would be used to map the IIR term. Mapping the finite impulse response term would be done directly through function composition.

If N is strictly greater than M, the numerator coefficients are zero-padded such that the numerator and denominator polynomials are of the same order. The polynomials can then be represented as two ordered (N+1) $\times$ 1 vectors: $\boldsymbol{a} = \begin{bmatrix} a_N & a_{N-1} \cdots a_0 \end{bmatrix}^T$ and $\boldsymbol{b} = \begin{bmatrix} b_N & b_{N-1} \cdots b_0 \end{bmatrix}^T$.

In the specific case of the forward second transform in Eq. (28), Eq. (28) is substituted into Eq. (35), and the numerator and denominator are scaled by $(s^2 + \Omega_o^2)^N$. The mapped IIR transfer function is

$$H'(s) = \frac{b_N\gamma^N s^N + b_{N-1}\gamma^{N-1}s^{N-1}(s^2+\Omega_o^2)^1 \cdots + b_0(s^2+\Omega_o^2)^N}{a_N\gamma^N s^N + a_{N-1}\gamma^{N-1}s^{N-1}(s^2+\Omega_o^2)^1 \cdots + a_0(s^2+\Omega_o^2)^N}. \quad (36)$$

The binomial theorem is then used to expand the $(s^2 + \Omega_o^2)^n,\ n = 0, 1, \ldots, N$ terms

$$(s^2 + \Omega_o^2)^n = \sum_{k=0}^{n} \binom{n}{k} s^{2k}\Omega_o^{2(n-k)}, \quad (37)$$

and powers of s represent a row permutation mapping the original coefficients to the correct order transformed coefficients. The transform can then be represented as a (2N+1) $\times$ (N+1) rectangular transformation matrix $\boldsymbol{A}$, which maps an (N+1) $\times$ 1 vector of general coefficients $\boldsymbol{c}$, representing either $\boldsymbol{a}$ or $\boldsymbol{b}$, to a (2N+1) $\times$ 1 vector of mapped coefficients $\boldsymbol{\kappa}$.

$$\boldsymbol{A}\boldsymbol{c} = \boldsymbol{\kappa}. \quad (38)$$

$\boldsymbol{A}$ is

$$\boldsymbol{A}_{(N-n+2k,n)} = \gamma^{(N-n)}\binom{n}{k}\Omega_o^{2(n-k)},\ k = 0, 1, \ldots, n,\ n = 0, 1, \ldots N \quad (39)$$

expressed in terms of its columns n. The formulation in Eq. (39) can also be used to apply the first transform Eq. (26) by swapping Ω_o^2 for $-\Omega_o^2$ and replacing γ with $-2\Omega_o\Omega_c$.

The row permutations that define $\boldsymbol{A}$ result in its columns being independent. $\boldsymbol{A}$ thus has full column-rank. As a result, a generalized inverse matrix $\boldsymbol{A}^+$ can be derived, corresponding to the Moore-Penrose pseudo-inverse.

$$\boldsymbol{A}^+\boldsymbol{\kappa} = \boldsymbol{c}. \quad (40)$$

This generalized inverse will be a least-squares approximation of the inverse transform in the coefficient space. As mentioned, this generalized inverse allows for numerically representation of the inverse transform without fractional powers that would appear in an analytic representation. Other common spectral transform matrix representations are shown in Table 4 in APPENDIX A.

6 GEOMETRY OF THE FIRST AND SECOND TRANSFORMS

The first transform [Eq. (28)] has now been derived, which maps a segment of the frequency axis back to the frequency axis twice. The inverse second transform, represented by a generalized inverse matrix, has also been derived. However, Applying the generalized inverse is not possible unless the mapped coefficients are within the column space of the forward transformation matrix.

Thankfully, because of the similarity between the first and forward second transform, the mapped coefficients can be placed into the column space of the second forward transformation matrix by manipulating the poles and zeros of the mapped system. More specifically, all the poles and zeros on the right half of the s-plane need to be reflected to the left half of the s-plane. This operation has the added benefit of stabilizing the response following the unstable first transform. Why reflecting the poles and zeros of the mapped system is necessary can be observed by examining the mapped geometry created by the two transforms.

6.1 Geometry of the First Transform

To understand the geometry of the first transform, consider how frequencies are mapped above the critical frequency Ω_o. Specifically, consider how a point $s = \frac{\Omega_o^2}{s}$ is mapped by the first transform in Eq. (26).

$$G_1\left(\frac{\Omega_o^2}{s}\right) = -\frac{2\Omega_o\Omega_c\frac{\Omega_o^2}{s}}{\left(\frac{\Omega_o^2}{s}\right)^2 - \Omega_o^2} = -G_1(s). \quad (41)$$

Thus, in the mapped space, any frequency $\Omega < \Omega_o$ has a corresponding frequency pair at $\frac{\Omega_o^2}{\Omega} > \Omega_o$, in which the magnitude and phase response are equivalent. The phase response, maybe counterintuitively, is the equivalent because factoring in $s = j\Omega$ imposes another change of sign.

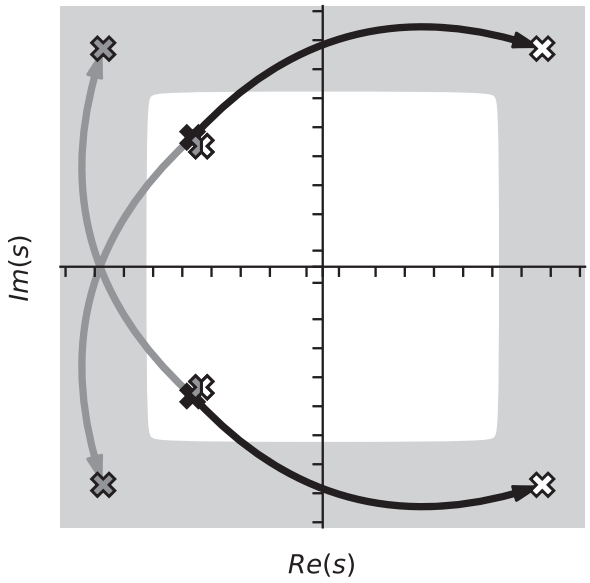

Fig. 5. A pair of complex conjugate poles (black) mapped by the first transform (white) with $\Omega_c = \Omega_o$ and by second forward transform (gray) with $\gamma = 2\Omega_o^2$. Axes are on a symbolic logarithmic scale. The area in gray represents values with radii $>\Omega_o$. The first transform will map poles across the $j\Omega$-axis, whereas the second transform will preserve the original stability.

From Eq. (42), it follows that any pole or zero with $|R_i| < \Omega_o$ (using R for root) has a corresponding reciprocal and negative pair at $-\Omega_o^2/R_i$. As a result, a system transformed by the first transform will have poles and zeros on both sides of the $j\Omega$-axis as shown in Fig. 5. An exception is in the case when the poles or zeros lie on the $j\Omega$-axis.

6.2 Geometry of the Second Transform

Again, consider a point $s = \frac{\Omega_o^2}{s}$ but now mapped by the forward second transform in Eq. (28).

$$G_2\left(\frac{\Omega_o^2}{s}\right) = \frac{\gamma\frac{\Omega_o^2}{s}}{\left(\frac{\Omega_o^2}{s}\right)^2 + \Omega_o^2} = G_2(s). \tag{42}$$

In comparison to the first transform, any frequency $\Omega < \Omega_o$ has a corresponding frequency pair at $\frac{\Omega_o^2}{\Omega} > x\Omega_o$, in which the magnitude response is equivalent, but the phase response is inverted.

For any pole or zero with $|R_i| < \Omega_o$, there is a corresponding reciprocal and *non-negative* pair at Ω_o^2/R_i. As a consequence, the forward second transform is stability preserving, whereas the first transform, as expected, is not.

Fig. 5 compares a set of complex conjugate poles mapped by the first transform with $\Omega_c = \Omega_o$ and the forward second transform with $\gamma = 2\Omega_o^2$. The mapped set of four roots are similar, but the first transform has reflected the roots with $|R_i| > \Omega_o$ across the $j\Omega$-axis. It can be seen that the first transform can be made to agree with the second by reflecting the unstable poles back across the $j\Omega$-axis.

For a system mapped with the first transform, reflecting the poles and zeros to the left-half of the s-plane causes the geometry of the mapped space to match that of the forward second transform. The coefficients will appear as if they were mapped with the forward second transform, and the generalized inverse matrix can be applied. Note the zeros could be flipped to the right-half plane and still match the geometry of the second transform. Doing so would produce a maximum phase system.

Reflecting the poles and zeros across the $j\Omega$-axis maintains the system's amplitude response but distorts the phase response near the Nyquist limit. Phase distortion near the Nyquist limit is an expected outcome in the discretization process by nature of the discrete-time domain, and the distortion introduced by the pole and zero reflecting process marginally adds to said distortion in exchange for a better-matched magnitude response.

After enforcing the geometry of the second transform on the coefficients mapped by the first transform, the generalized inverse can be applied, and the desired pre-mapping can be produced in Eq. (12).

6.3 Biquadratic Filter Example

As an example demonstrating the necessity of pole and zero flipping, consider the case of a continuous-time biquadratic filter,

$$\frac{b_2 s^2 + b_1 s + b_0}{a_2 s^2 + a_1 s + a_0}, \tag{43}$$

mapped by the forward second transform in Eq. (28). Using the definition in Eq. (39), or through direct derivation, the coefficient transform matrix

$$\begin{bmatrix} 0 & 0 & 1 \\ 0 & \gamma & 0 \\ \gamma^2 & 0 & 2\Omega_o^2 \\ 0 & \Omega_o^2\gamma & 0 \\ 0 & 0 & \Omega_o^4 \end{bmatrix} \begin{bmatrix} c_2 \\ c_1 \\ c_0 \end{bmatrix} = \begin{bmatrix} \kappa_4 \\ \kappa_3 \\ \kappa_2 \\ \kappa_1 \\ \kappa_0 \end{bmatrix} \tag{44}$$

is derived, where $\boldsymbol{c}_i$ and $\boldsymbol{\kappa}_i$ generally represent the numerator or denominator coefficients. To invert this transform, the mapped coefficients $\boldsymbol{\kappa}$ must be in the column space of the forward transform. This is achieved by enforcing

$$\kappa_0 = \Omega_o^4 \kappa_4, \tag{45}$$

$$\kappa_1 = \Omega_o^2 \kappa_3. \tag{46}$$

These constraints are met if roots of the mapped fourth-order polynomial have reciprocal pairs about Ω_o^2: for every possibly complex pair of roots r_1 and r_2, there must also exist roots at Ω_o^2/r_1 and Ω_o^2/r_2. As proof, consider a polynomial $P(s)$ with roots $\{r_1, r_2, \Omega_o^2/r_1, \Omega_o^2/r_2\}$

$$P(s) = (s - r_1)\left(s - \frac{\Omega_o^2}{r_1}\right)(s - r_2)\left(s - \frac{\Omega_o^2}{r_2}\right). \tag{47}$$

Expanding this polynomial,

$$P(s) = s^4 + p_3 s^3 + p_2 s^2 + \Omega_o^2 p_3 s + \Omega_o^4, \tag{48}$$

can be seen, where

$$p_3 = -\left(r_1 + r_2 + \frac{\Omega_o^2}{r_1} + \frac{\Omega_o^2}{r_2}\right), \tag{49}$$

$$p_2 = \frac{\Omega_o^4}{r_1 r_2} + \Omega_o^2 \left(2 + \frac{r_1}{r_2} + \frac{r_2}{r_1}\right) + 1. \quad (50)$$

Enforcing that the mapped roots have non-negative reciprocal pairs achieves the same criteria in Eqs. (45) and (46) for the coefficient vector to be in the column space. Thus, for these transforms, there is an equivalence between enforcing the geometry of the second transform and placing the coefficient vector in the column space of the forward second transformation matrix.

7 THE NYQUIST BAND TRANSFORM

To recapitulate SEC. 2: the Nyquist band transform provides a method to pre-map a continuous-time IIR filter response by using a series of transforms prior to discretization with the standard bilinear transform. The proposed method can be broken down into the following set of steps:

1 Apply the first transform in Eq. (26) to map a truncated segment of a prototype filter's continuous-time frequency response back to the continuous-time frequency axis twice.
2 Stabilize and enforce minimum or maximum phase on the mapped system.
3 Apply the inverse second transform of Eq. (28) to the stabilized and mapped coefficients to produce the desired pre-mapping in Eq. (11).
4 Discretize with the standard bilinear transform Eq. (3).

Because the transform doubles and then halves the order of the original system, the proposed transform is order-preserving. The pole and zero reflection along with the stability-preserving qualities of the second and bilinear transforms ensure the method is stability preserving.

8 IMPLEMENTATION

In practice, discretizing using the proposed transform is computationally expensive. Higher-order filters require correspondingly sized transformation matrices. As N increases in Eq. (39), so does the value of its largest element as determined by $\Omega_o^{2(n-k)}$ and $\gamma^{(N-n)}$. Because the smallest non-zero element will be unity, larger transformation matrices will have increasingly large condition numbers [39]. As a result, the transformation matrices will have numerical stability issues, making their application and the computation of the generalized inverse unreliable. Additionally, it is computationally expensive if the parameters of either

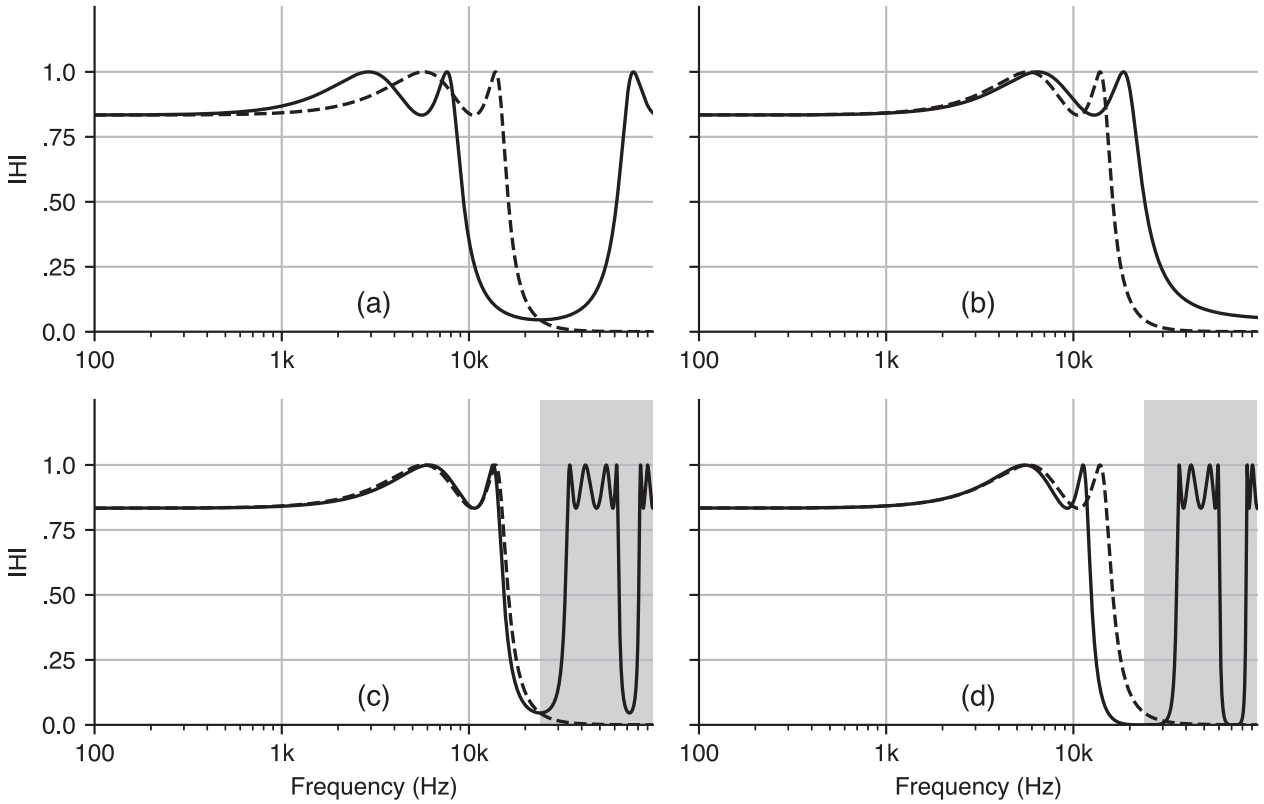

Fig. 6. Nyquist band transform process in (a)–(c) compared to discretization with the bilinear transform (d). In (a), the fourth-order Chebyshev filter prototype (dashed line) is transformed by the first transform in Eq. (26). In (b), the inverse second transform in Eq. (28) is applied to suitably pre-map the frequency axis. In (c), the pre-mapped response is discretized with the bilinear transform. The result is compared to naive discretization with the bilinear transform in (d). In this example, $f_s = 48$ kHz, and frequencies above the Nyquist band are indicated by the gray background. Notice that the mapped filters responses (solid) in (a)–(c) replicate the behavior of the prototype filter only up to the Nyquist limit.

transform, Ω_o and γ, change. Recomputing the transform matrix from Eq. (39) is computationally expensive, and a new generalized inverse must be computed.

The final computationally expensive step in the proposed method is computing the pole and zero locations to perform the necessary pole and zero reflection step. The first two issues are remedied by separating the parameters Ω_o and γ from the form of the first and second transform. A computation method to find the pole and zero locations is shown.

8.1 Separation of Parameters

The parameters Ω_o and Ω_a are separated from the form of first and second transforms by decomposing the transforms into a combination of spectral transforms.

8.1.1 Decomposition of the First Transform

To separate out the parameters Ω_o from the first transform, Eq. (26) is rewritten with $\Omega_c = \Omega_o$ as a series of three transforms:

$$G_1(s) = \left(\hat{G}_{N_1} \circ \hat{G}_{D_1} \circ G_{\Omega_o \to 1}\right)(s). \tag{51}$$

The right-most transform in Eq. (51) scales the Nyquist limit in angular frequencies to unity:

$$G_{\Omega_o \to 1}(s) = \frac{1}{\Omega_o} s. \tag{52}$$

This "normalizes" the first transform allowing to set $\Omega_o = 1$. Using the hat operator to connote $\Omega_o = 1$ normalization, the normalized first transform is

$$\hat{G}_1(s) = \frac{-2s}{s^2 - 1}, \tag{53}$$

and the transform is no longer dependent on Ω_o. The left two transforms in Eq. (51) are a result of decomposing the normalized first transform into two separate transforms:

$$\hat{G}_1(s) = (\hat{G}_{N_1} \circ \hat{G}_{D_1})(s), \tag{54}$$

with

$$\hat{G}_{N_1}(s) = -2s, \tag{55}$$

$$\hat{G}_{D_1}(s) = \frac{s}{s^2 - 1}. \tag{56}$$

The subscript N_1 implies the numerator coefficient of $\hat{G}_1$. D_1 implies the denominator coefficient of $\hat{G}_1$ because the numerator coefficient is unity.

The corresponding matrix transformation to map a vector of (N+1) $\times$ 1 general coefficients $\boldsymbol{c}$ to a (2N+1) $\times$ 1 set of mapped coefficients $\boldsymbol{\kappa}$ is now three separate matrix transformations:

$$\hat{\boldsymbol{N}}_1 \hat{\boldsymbol{D}}_1 \boldsymbol{F} \boldsymbol{c} = \boldsymbol{\kappa}, \tag{57}$$

where

$$\hat{\boldsymbol{N}}_{1(n,n)} = (-2)^{(2N-n)},\ n = 0, 1, \ldots 2N, \tag{58}$$

$$\hat{\boldsymbol{D}}_{1(N-n+2k,n)} = \binom{n}{k} (-1)^{(n-k)},\ k = 0, 1, \ldots, n \quad n = 0, 1, \ldots N, \tag{59}$$

$$\boldsymbol{F}_{(n,n)} = \left(\frac{1}{\Omega_o}\right)^{(N-n)},\ n = 0, 1, \ldots N. \tag{60}$$

Through this composition, $\hat{\boldsymbol{N}}_1$ and $\hat{\boldsymbol{D}}_1$ are now constant value matrices and can be computed prior to processing. The first transform is only parameterized using $\boldsymbol{F}$, which is a diagonal matrix that can be swiftly computed if the sampling rate of the system changes.

8.1.2 Decomposition of the Second Transform

The same decomposition done to the first transform can be applied to the forward second transform as well:

$$G_2(s) = \left(\hat{G}_{N_2} \circ \hat{G}_{D_2} \circ G_{\Omega_o \to 1}\right)(s), \tag{61}$$

with

$$\hat{G}_{N_2}(s) = \hat{\gamma} s, \tag{62}$$

$$\hat{G}_{D_2}(s) = \frac{s}{s^2 + 1}, \tag{63}$$

and $G_{\Omega_o \to 1}(s)$ as before. A normalized γ parameter, $\hat{\gamma}$, that is computed by recognizing that γ is in units of $(\text{rad/s})^2$. is now required. The result in Eq. (34) is divided by Ω_o^2 to obtain

$$\hat{\gamma} = 2 \frac{\frac{2}{T} \tan\left(\frac{\Omega_a T}{2}\right)}{\Omega_a} \sqrt{1 - \left(\frac{\Omega_a T}{\pi}\right)^2}. \tag{64}$$

The matrix representation of the forward second transform is

$$\hat{\boldsymbol{N}}_2 \hat{\boldsymbol{D}}_2 \boldsymbol{F} \boldsymbol{c} = \boldsymbol{\kappa}, \tag{65}$$

where

$$\hat{\boldsymbol{N}}_{2(n,n)} = (\hat{\gamma})^{(2N-n)},\ n = 0, 1, \ldots 2N, \tag{66}$$

$$\hat{\boldsymbol{D}}_{2(N-n+2k,n)} = \binom{n}{k} (1)^{(n-k)},\ k = 0, 1, \ldots, n \quad n = 0, 1, \ldots N. \tag{67}$$

The inverse second transform is applied by taking the inverse transforms of Eq. (65). To map a set of (2N+1) $\times$ 1 coefficients $\boldsymbol{\kappa}$ to a set of (N+1) $\times$ 1 coefficients $\boldsymbol{c}$:

$$\boldsymbol{F}^{-1} \hat{\boldsymbol{D}}_2^{+} \hat{\boldsymbol{N}}_2^{-1} \boldsymbol{\kappa} = \boldsymbol{c}. \tag{68}$$

The inverses of the diagonal matrices, $\boldsymbol{F}$ and $\hat{\boldsymbol{N}}_2$, are easily computed by replacing the diagonal elements with their reciprocals. $\hat{\boldsymbol{D}}_2$ is a constant value matrix, and the generalized inverse can be pre-computed ahead of time and stored before processing. Additionally, computing the generalized inverse $\hat{\boldsymbol{D}}_2^{+}$ is more numerically robust than $\boldsymbol{A}_2^{+}$ because it has a smaller condition number because of the decomposition described above. If the sampling rate changes, $\hat{\boldsymbol{N}}_2^{-1}$ and $\boldsymbol{F}^{-1}$ need to be recomputed. If the transform is parameterized by some frequency of interested Ω_a that changes, only $\hat{\boldsymbol{N}}_2^{-1}$ needs to be recomputed.

The algorithm for applying the Nyquist band transform is provided in Table 1. The size of the matrices can be determined by the largest system being discretized. Any

Table 1. Nyquist band transform algorithm.

Pre-computation:
i. Compute the constant matrices: $\hat{\boldsymbol{N}}_1$, $\hat{\boldsymbol{D}}_1$, and the generalized inverse $\hat{\boldsymbol{D}}_2^{+}$. ii. If the sampling rate is known, compute $\boldsymbol{F}$ and $\boldsymbol{F^{-1}}$ iii. If Ω_a is known, compute $\hat{\boldsymbol{N}}_2^{-1}$
Coefficient processing:
1. Apply the first transform in Eq. (57) on the coefficient vectors $\boldsymbol{a}$ and $\boldsymbol{b}$ to generated mapped coefficients $\boldsymbol{\kappa}_a$ and $\boldsymbol{\kappa}_b$ 2. Stabilize the mapped coefficients $\boldsymbol{\kappa}_a$ and enforce minimum/maximum phase on $\boldsymbol{\kappa}_b$ 3. Apply the inverse second transform in Eq. (68) on $\boldsymbol{\kappa}_a$ and $\boldsymbol{\kappa}_b$ to produce the pre-mapped coefficients $\boldsymbol{a}'$ and $\boldsymbol{b}'$ 4. Discretize with the bilinear transform.
If f_s or Ω_a change:
1. Update $\boldsymbol{F}$, $\boldsymbol{F^{-1}}$, or $\hat{\boldsymbol{N}}_2^{-1}$, respectively.

lower-order polynomials coefficient vectors can be zero-padded at the cost of increased computation.

8.2 Root Finding and System Stabilization

Another computational bottleneck in the process is stabilizing and enforcing the minimum or maximum phase before applying the inverse second transform. Doing so necessitates finding the poles and zeros of the transformed system.

For low-order systems, the roots can be found directly through algebraic methods or examination of the transformation matrices. However, for an arbitrary or higher-order system, a companion matrix method [40] can be used to find the roots. Given a mapped vector $\boldsymbol{\kappa}$, the corresponding companion matrix is

$$\boldsymbol{K} = \begin{bmatrix} 0 & 0 & \dots & 0 & -\kappa_0/\kappa_{2N} \\ 1 & 0 & \dots & 0 & -\kappa_1/\kappa_{2N} \\ 0 & 1 & \dots & 0 & -\kappa_2/\kappa_{2N} \\ \vdots & \vdots & \ddots & \vdots & \vdots \\ 0 & 0 & \dots & 1 & -\kappa_{2N-1}/\kappa_{2N} \end{bmatrix}. \tag{69}$$

The eigenvalues of $\boldsymbol{K}$ correspond to the roots of the polynomial. This method is available in Python `NumPy` library and MATLAB using `roots`. A method in C++ is provided by the Eigen library.[1] Following root finding and stabilization, new polynomial coefficients can be iteratively computed from the roots using Viète's formula [41].

9 OPTIMIZATION OF THE γ-PARAMETER

If there is no a priori information of the system being discretized, it may be desirable to generically minimize frequency warping across the entire audio spectrum. An optimal value of γ can be found by minimizing the mapped frequency error,

$$\min_{\gamma} |\Omega_{NB}(\Omega, \gamma, f_s) - \Omega|, \tag{70}$$

across the entire audio spectrum. Here, Ω_{NB} is the frequency warping caused by the Nyquist band transform and is determined by a parameter γ and the sampling rate. Ω_{NB} is found by evaluating the overall frequency warpings through the discretization process:

$$\Omega_{NB}(\Omega) = (|g_1| \circ |g_2|^{-1} \circ |g_{BT}|)(\Omega), \tag{71}$$

$$|g_1|(\Omega) = \frac{2\Omega_o^2 \Omega}{-\Omega^2 - \Omega_o^2}, \tag{72}$$

$$|g_2|(\Omega) = \frac{\gamma \Omega}{-\Omega^2 + \Omega_o^2}. \tag{73}$$

As before, $\Omega_o = \pi f_s$, and $|g_{BT}(\Omega)|$ is the frequency warping of the bilinear transform in Eq. (4). The optimization can incorporate a perceptual weighting, such as one based on the Bark frequency scale, to minimize frequency warping over a perceptually relevant band of frequencies

$$\min_{\gamma} |w(\Omega) \cdot (\Omega_{NB}(\Omega, \gamma, f_s) - \Omega)|. \tag{74}$$

A suggested Bark scale-based weighting is determined by the reciprocal of the number of bins in each bandwidth. Assuming a linearly spaced set of frequencies is being optimized over, compute the Bark band of each linear frequency bin and determine the number of linear frequency bins in said Bark band. The weight at each frequency bin will be the reciprocal of the number of bins in that Bark band.

$$w_{\text{Bark}}(\Omega) = \frac{1}{\#\text{ Bins in at Bark } \left(\frac{\Omega}{2\pi}\right) \text{ band}}, \tag{75}$$

where Bark $\left(\frac{\Omega}{2\pi}\right)$ determines the Bark band from a frequency in hertz. The approximation from [42] is utilized.

Following this optimization, the normalized $\hat{\gamma} = \gamma / \Omega_o^2$ is found to replace Eq. (64). A table of $\hat{\gamma}$ values for common sampling rates using the Bark weighting above are given in Table 2.

Table 2. Bark-weighted optimal $\hat{\gamma}$ values for common sampling rates.

Sampling Rate (Hz)	$\hat{\gamma}$
44,100	2.059
48,000	2.058
96,000	2.042
192,000	2.024

In Fig. 7, the optimization results are compared to a γ value using Eq. (34), in which Ω_a is the geometric mean of the pole frequencies, which is a heuristic approach to determining a relevant frequency of interest used in [43]. Other perceptually motivated frequency weights could be used in the optimization to further tune the results.

[1] https://eigen.tuxfamily.org/index.php?title\=Main_Page.

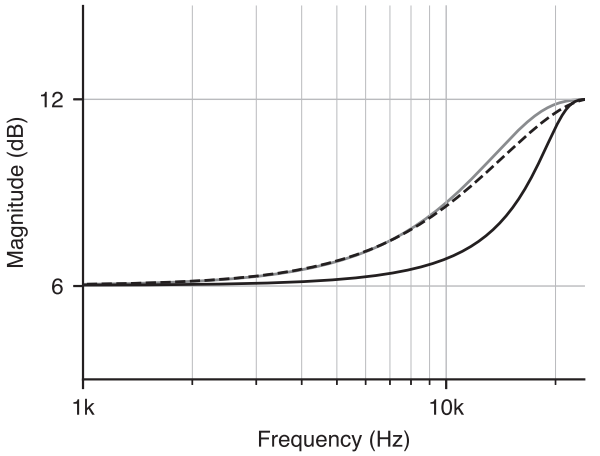

Fig. 7. Comparison of a peaking filter prototype (gray) with center frequency 26 kHz transformed discretized using an optimized value $\hat{\gamma} = 2.058$ (dashed line) compared matching a singular frequency across the discretization (dashed line). The response is discretized with a sampling rate of 48 kHz.

10 EXAMPLE

An analog graphic equalizer can be constructed based on the circuit shown on the left of Fig. 8. This topology can be found in pedals such as the MXR M108 and MXR M109 [44, 45]. The graphic equalizer contains a series of n second-order active band-pass–filter gains, whose gains are controlled by potentiometers P_n and whose center frequencies are determined by R_{n1}, R_{n2}, C_{n1}, and C_{n2}. An additional high-pass filter section is defined by P_s, R_s, and C_s. In Fig. 8, the circuit has been simplified to focus on the response of each individual section.

For this analysis, a single section (on the right of the Fig. 8) is examined independently by assuming the op-amps are ideal and their high input impedance allows ignoring any coupling between sections. The potentiometer is represented as a voltage divider [46]. Through nodal analysis, the following continuous-time transfer time transfer function is derived:

$$H(s) = \frac{b_2 s^2 + b_1 s}{a_2 s^2 + a_1 s + a_0}, \tag{76}$$

for which the coefficients are

$$b_2 = R_o(R_{P1})(C_1 C_2 R_2), \tag{77}$$

$$b_1 = R_o(R_{P1})C_1, \tag{78}$$

$$a_2 = (R_{P1} + R_{P2})(C_1 C_2 R_1 R_2) + (R_{P1} R_{P2})(C_1 C_2 R_2), \tag{79}$$

$$a_1 = (R_{P1} + R_{P2})(C_1 R_2 + C_2 R_2) + (R_{P1} R_{P2})C1, \tag{80}$$

$$a_0 = R_{P1} + R_{P2}. \tag{81}$$

And for the high-pass filter section, the transfer function is

$$H_s(s) = \frac{b_1 s}{a_1 s + a_0}, \tag{82}$$

$$b_1 = R_o(R_{PS1})C_s, \tag{83}$$

$$a_1 = (R_{PS1} + R_{PS2})(2C_s R_s) + (R_{PS1} R_{PS2})C_s, \tag{84}$$

$$a_0 = R_{PS1} + R_{PS2}. \tag{85}$$

It is not possible to use techniques as in [47, 24] when discretizing these filters because multiple parameters of the

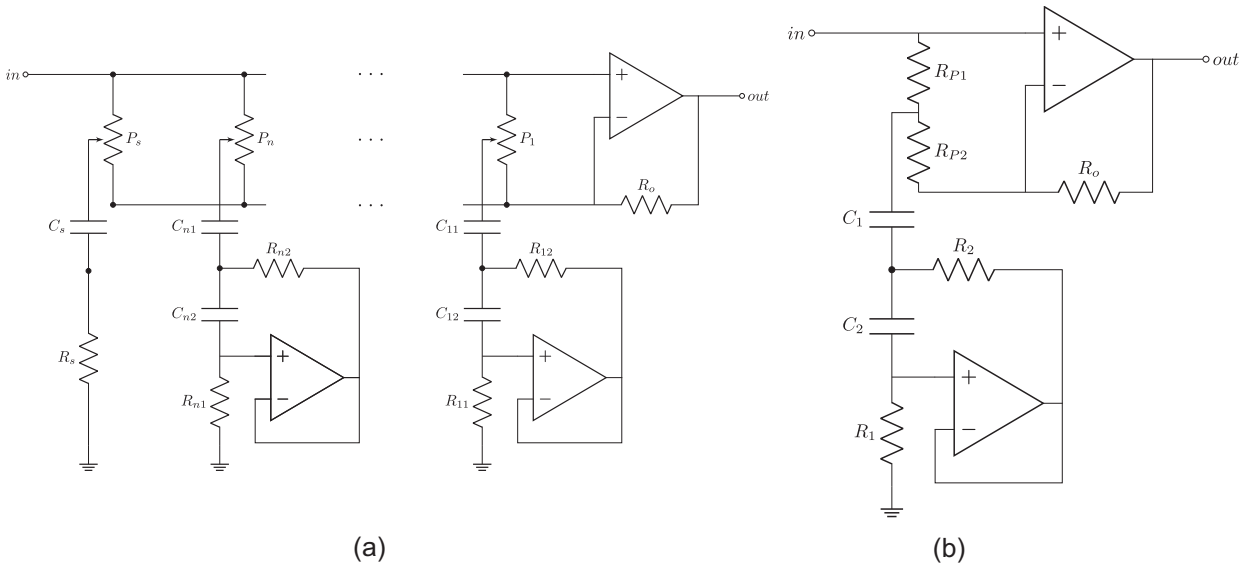

Fig. 8. (a) Entire simplified graphic equalizer diagram with n sections and one shelving section. (b) Single section with potentiometer represented as a voltage divider.

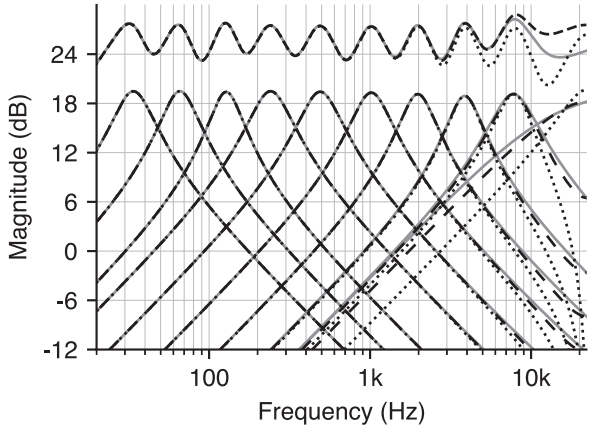

Fig. 9. Comparison between the continuous-time response of a ten-band graphic equalizer (gray line), pre-warped bilinear transform discretization (dotted line), and the proposed method (dashed line). The combined response of all graphic equalizer sections is shown with a +6-dB offset.

Table 3. Component values for a ten-band graphic equalizer.

Section (n)	f_0 (Hz)	R_1 (Ω)	C_1 (nF)	C_2 (nF)
1	31.2	100,000	4,700	100
2	62.5	120,000	2,200	47
3	125	100,000	1,000	33
4	250	91,000	680	15
5	500	68,000	330	10
6	1,000	51,000	150	6.8
7	2,000	43,000	68	4.7
8	4,000	33,000	33	3.3
9	8,000	27,000	22	1.5
Section	f_0 (Hz)	R_s (Ω)	C_s (nF)	
N/A	16,000	470	22	

filter section depend on the position of the potentiometer and the filter cannot be modeled as a parametric section combined with a linear gain.

The component values and designed center frequency f_0 for a ten-band graphic equalizer are shown in Table 3 with $R_2 = 470\ \Omega$ for all sections. For each section, the internal potentiometer resistances are assumed to be equal and set to 100 Ω. The continuous-time response of the transfer functions in Eqs. (76) and (82) is compared against the discrete-time response formed from the proposed method and pre-warped bilinear transform. The sampling rate of this system is 44.1 kHz.

The digital response produced by the bilinear transform is generally suitable for the lower eight band-pass sections but deviates noticeably in the last band-pass section and final high-pass section. The bilinear transform response of the high-pass section deviates from the continuous-time response by approximately 6 dB because of frequency warping. The high-frequency response of the lower band-pass sections also suffers from warping. As a result, the total graphic equalizer response formed from the bilinear transformed sections deviates from the continuous-time response at frequencies as low as 4 kHz, which is well within the audibility band. The total graphic equalizer response formed from the sections discretized with the proposed method matches the response for some additional 4 kHz before deviating significantly from the continuous-time response.

11 CONCLUSION

In this article, a new discretization method based on conformal maps has been presented. The proposed method operates by pre-mapping the frequency spectrum between dc and the Nyquist limit to the entire frequency axis prior to discretization. Following discretization with the bilinear transform, only the set of digitally realizable frequencies in the Nyquist band are mapped to the z-plane. The composite magnitude frequency-warping for the discretization, including the bilinear transform, appears in Fig. 1.

Practical solutions are proposed to optimize the transform parameters for minimum frequency wrapping and to ensure a numerically stable implementation. The authors believe this method to be useful in virtual analog modeling and in general for discrete-time representations of analog filters near the Nyquist limit.

12 ACKNOWLEDGMENT

The authors would like to thank Julius O. Smith, III, and Dirk Roosenburg for discussions on the presentation of this article. The authors would like to give thanks to the anonymous reviewer for their indispensable comments throughout the review process.

13 REFERENCES

[1] A. V. Oppenheim, R. W. Schafer, and J. R. Buck, *Discrete-Time Signal Processing*, Prentice-Hall Signal Processing Series (Prentice-Hall, Englewood Cliffs, NJ, 1999), 2nd ed.

[2] K. Steiglitz, *A Digital Signal Processing Primer: With Applications to Computer Music* (Addison-Wesley, Reading, MA, 1994).

[3] S. K. Mitra, *Digital Signal Processing: a Computer-Based Approach* (McGraw-Hill Higher Education, New York, NY, 2006), 3rd ed.

[4] E. C. Ifeachor and B. W. Jervis, *Digital Signal Processing: A Practical Approach* (Pearson Education, Essex, UK, 2002), 2nd ed.

[5] S. J. Orfanidis, *Introduction to Signal Processing* (Pearson Education, Upper Saddle River, NJ, 1996).

[6] III J. O. Smith, *Introduction to Digital Filters With Audio Applications* (W3K Publishing, 2007).

[7] S. A. White, "Design of a Digital Biquadratic Peaking or Notch Filter for Digital Audio Equalization," presented at the *78th Convention of the Audio Engineering Society* (1985 May), paper 2230.

[8] J. Backman, "Digital Realisation of Phono (RIAA) Equalisers," *IEEE Trans. Consum. Electron.*, vol. 37, no. 3, pp. 659–662 (1991 Aug.). http://dx.doi.org/10.1109/30.85582.

[9] F. G. Germain and K. J. Werner, "Optimizing Differentiated Discretization for Audio Circuits Beyond Driving Point Transfer Functions," in *Proceedings of the IEEE Workshop on Applications of Signal Processing to Audio and Acoustics (WASPAA)*, pp. 384–388 (New Paltz, NY) (2017 Oct.). http://dx.doi.org/10.1109/WASPAA.2017.8170060.

[10] U. Zölzer, *Digital Audio Signal Processing* (Wiley, Chippenham, UK, 2008), 2nd ed.

[11] V. Välimäki and J. D. Reiss, "All About Audio Equalization: Solutions and Frontiers," *Appl. Sci.*, vol. 6, no. 5, paper 129 (2016 May). https://doi.org/10.3390/app6050129.

[12] III J. O. Smith, *Physical Audio Signal Processing* (W3K Publishing, 2010).

[13] T. S. Stilson, *Efficiently-Variable Non-Oversampled Algorithms in Virtual-Analog Music Synthesis: A Root-Locus Perspective*, Ph.D. thesis, Stanford University, Stanford, CA (2006 Jun.).

[14] III, J. O. Smith and J. S. Abel, "The Bark Bilinear Transform," in *Proceedings of the IEEE Workshop on Applications of Signal Processing to Audio and Acoustics (WASPAA)*, pp. 202–205 (New Paltz, NY) (1995 Oct.). http://dx.doi.org/10.1109/ASPAA.1995.482991.

[15] A. W. Soewito, *Least Square Digital Filter Design in the Frequency Domain*, Ph.D. thesis, Rice University, Houston, TX (1990 Dec.).

[16] E. C. Levy, "Complex-Curve Fitting," *IRE Trans. Automat. Contr.*, vol. AC-4, no. 1, pp. 37–43 (1959 May). http://dx.doi.org/10.1109/TAC.1959.6429401.

[17] L. B. Jackson, "Frequency-Domain Steiglitz-McBride Method for Least-Squares IIR Filter Design, ARMA Modeling, and Periodogram Smoothing," *IEEE Signal Process. Lett.*, vol. 15, pp. 49–52 (2008 Jan.). http://dx.doi.org/10.1109/LSP.2007.910320 .

[18] R. Storn, "Designing Nonstandard Filters With Differential Evolution," *IEEE Signal Process. Mag.*, vol. 22, no. 1, pp. 103–106 (2005 Jan.). http://dx.doi.org/10.1109/MSP.2005.1407721.

[19] M. Karjalainen, A. Härmä, and U. K. Laine, "Realizable Warped IIR Filters and Their Properties," in *Proceedings of the IEEE International Conference on Acoustics, Speech, and Signal Processing*, vol. 3, pp. 2205–2208 (Munich, Germany) (1997 Apr.). http://dx.doi.org/10.1109/ICASSP.1997.599488.

[20] S. Sarkka and A. Huovilainen, "Accurate Discretization of Analog Audio Filters With Application to Parametric Equalizer Design," *IEEE Trans. Audio Speech Lang. Process.*, vol. 19, no. 8, pp. 2486–2493 (2011 Nov.). https://doi.org/10.1109/TASL.2011.2144970.

[21] F. G. Germain and K. J. Werner, "Design Principles for Lumped Model Discretisation Using Möbius Transforms," in *Proceedings of the 15th International Conference on Digital Audio Effects (DAFx) International Conference on Digital Audio Effects (DAFx)15th International Conference on Digital Audio Effects (DAFx) International Conference on Digital Audio Effects (DAFx)*, paper 52 (Trondheim, Norway) (2015 Nov.).

[22] F. G. Germain, "Practical Virtual Analog Modeling Using MÖbius Transforms," in *Proceedings of the 24th International Conference on Digital Audio Effects (DAFx) International Conference on Digital Audio Effects (DAFx)*, pp. 49–56 (Online) (2021 Sep.). http://dx.doi.org/10.23919/DAFx51585.2021.9768245.

[23] M. A. Al-Alaoui, "Novel Approach to Analog-to-Digital Transforms," *IEEE Trans. Circuits Syst. I Regul. Pap.*, vol. 54, no. 2, pp. 338–350 (2007 Feb.). http://dx.doi.org/10.1109/TCSI.2006.885982.

[24] J. Sierra, "Digital Parametric Filters Beyond Nyquist Frequency," presented at the *147th Convention of the Audio Engineering Society* (2019 Oct.), paper 10224.

[25] C. Darabundit and R. Wedelich, "Generalized Digital Second Order Systems Beyond Nyquist," presented at the *149th Convention of the Audio Engineering Society* (2020 Oct.), e-Brief 631.

[26] S. J. Orfanidis, "Digital Parametric Equalizer Design With Prescribed Nyquist-Frequency Gain," *J. Audio Eng. Soc.*, vol. 45, no. 6, pp. 444–455 (1997 Jun.).

[27] D. P. Berners and J. S. Abel, "Discrete-Time Shelf Filter Design for Analog Modeling," presented at the *115th Convention of the Audio Engineering Society* (2003 Oct.), paper 5939.

[28] M. Massberg, "Digital Low-Pass Filter Design With Analog-Matched Magnitude Response," presented at the *131st Convention of the Audio Engineering Society Convention* (2011 Oct.), paper 8551.

[29] Z. Nehari, *Conformal Mapping* (Dover Publications, New York, NY, 1952).

[30] M. Karjalainen, A. Härmä, U. K. Laine, and J. Huopaniemi, "Warped Filters and Their Audio Applications," in *Proceedings of the Workshop on Applications of Signal Processing to Audio and Acoustics (WASPAA)* (New Paltz, NY) (1997 Oct.). http://dx.doi.org/10.1109/ASPAA.1997.625615.

[31] E. Krüger and H. W. Strube, "Linear Prediction on a Warped Frequency Scale (Speech Processing)," *IEEE Trans. Acoust., Speech Signal Process.*, vol. 36, no. 9, pp. 1529–1531 (1988 Sep.). http://dx.doi.org/10.1109/29.90384.

[32] A. Härmä, M. Karjalainen, L. Savioja, et al., "Frequency-Warped Signal Processing for Audio Applications," *J. Audio Eng. Soc.*, vol. 48, no. 11, pp. 1011–1029 (2000 Nov.).

[33] A. G. Constantinides, "Spectral Transformations for Digital Filters," *Proc. Inst. Electr. Eng.*, vol. 117, no. 8, pp. 1585–1590 (1970 Aug.). http://dx.doi.org/10.1049/piee.1970.0281.

[34] E. A. Guillemin, *Synthesis of Passive Networks; Theory and Methods Appropriate to the Realization and Approximation Problems* (Wiley, New York, NY, 1957).

[35] J. R. Ragazzini and L. A. Zadeh, "The Analysis of Sampled-Data Systems," *Trans. AIEE, Part II: Appl. Ind.*, vol. 71, no. 5, pp. 225–234 (1952 Nov.). http://dx.doi.org/10.1109/TAI.1952.6371274.

[36] E. Kanasewich, *Time Sequence Analysis in Geophysics* (The University of Alberta Press, Edmonton, Canada, 1981), 3rd ed.

[37] J. A. Moorer, "The Manifold Joys of Conformal Mapping: Applications to Digital Filtering in the Studio," *J. Audio Eng. Soc.*, vol. 31, no. 11, pp. 826–841 (1983 Nov.).

[38] A. M. Bush and D. C. Fielder, "Simplified Algebra for the Bilinear and Related Transformations," *IEEE Trans. Audio Electroacoust.*, vol. 21, no. 2, pp. 127–128 (1973 Apr.). http://dx.doi.org/10.1109/TAU.1973.1162448.

[39] G. Strang, *Introduction to Linear Algebra* (Wellesley-Cambridge Press, Wellesley, MA, 2016), 5th ed.

[40] A. Edelman and H. Murakami, "Polynomial Roots From Companion Matrix Eigenvalues," *Math. Comput.*, vol. 64, no. 210, pp. 763–776 (1995 Apr.). http://dx.doi.org/10.1090/S0025-5718-1995-1262279-2.

[41] B. L. van der Waerden, *Algebra: Volume I* (Springer, New York, NY, 1991), 1st ed.

[42] H. Traunmüller, "Analytical Expressions for the Tonotopic Sensory Scale," *J. Acoust. Soc. Am.*, vol. 88, no. 1, pp. 97–100 (1990 Jul.). http://dx.doi.org/10.1121/1.399849.

[43] C. C. Darabundit and J. S. Abel, "Conformal Maps for the Discretization of Analog Filters Near the Nyquist Limit," in *Proceedings of the 24th International Conference on Digital Audio Effects (DAFx)*, pp. 97–104 (Online) (2021 Sep.). http://dx.doi.org/10.23919/DAFx51585.2021.9768215.

[44] Dunlop, "MXR SIX BAND EQ: M109S," https://www.jimdunlop.com/mxr-six-band-eq/ (Accessed October 15, 2021).

[45] Dunlop, "MXR TEN BAND EQ: M108S," https://www.jimdunlop.com/mxr-ten-band-eq/ (Accessed October 15, 2021).

[46] B. Holmes and M. van Walstijn, "Potentiometer Law Modelling and Identification for Application in Physics-Based Virtual Analogue Circuits," in *Proceedings of the 22nd International Conference on Digital Audio Effect (DAFx)*, pp. 332-339 (Birmingham, UK) (2019 Sep.).

[47] S. J. Orfanidis, "High-Order Digital Parametric Equalizer Design," *J. Audio Eng. Soc.*, vol. 53, no. 11, pp. 1026–1024 (2005 Nov.).

A.1 SPECTRAL TRANSFORMS

Spectral transforms are normally used to design low-pass, high-pass, band-pass, and band-stop filters from prototype low-pass filters. Discrete-time all-pass transforms of these transforms are given in [33] and their continuous-time equivalents can be found using Eq. (14). These equivalents and their corresponding matrix representations are given in Eq. (14).

In all the transforms, B is the frequency mapped, in the first-order cases, to Ω_c, and in the second-order cases, to the lower and upper band edges Ω_1 and Ω_2. The quantity Ω_o is defined by $\Omega_o^2 = \Omega_1\Omega_2$ and is the center frequency of the pass-band or stop-band in the band-pass and band-stop transforms, respectively. The band-stop transform has the same form as the forward second transform shown in SEC. 5.

Table 4. Continuous-time spectral transforms.

Order	Transform	$G(s)$	Matrix Representation
1	Low-pass	$\frac{B}{\Omega_c}s = \gamma s$	$A_{(n,n)} = \gamma^{(N-n)}$
1	High-pass	$-B\Omega_c\frac{1}{s} = \gamma\frac{1}{s}$	$A_{(n,N-n)} = \gamma^{n}$
2	Band-pass	$\frac{B}{\Omega_2-\Omega_1}\frac{s^2+\Omega_o^2}{s} = \gamma\frac{s^2+d}{s}$	$A_{(n+2k,m)} = \gamma^{(N-n)}\binom{N-n}{k}d^{N-n-k}, k = 0,\ldots,N-n$
2	Band-stop	$B(\Omega_2-\Omega_1)\frac{s}{s^2+\Omega_o^2} = \gamma\frac{s}{s^2+d}$	$A_{(N-n+2k),n} = \gamma^{(N-n)}\binom{n}{k}d^{n-k}, k = 0,\ldots,n$

THE AUTHORS


Champ C. Darabundit

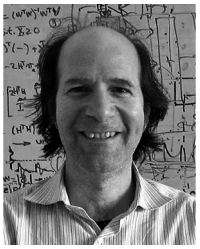
Jonathan S. Abel


David Berners

Champ C. Darabundit earned an M.A. in Music, Science, and Technology from the Center for Computer Research in Music and Acoustics (CCRMA) at Stanford University in 2022. He received a B.S. degree in Electrical Engineering and B.A. degree in Art and Design from the University of Southern California, Los Angeles, California, in 2020. His research interests are in filter design, virtual analog modeling, and physical modeling. He was previously a consultant at Eventide Inc.

•

Jonathan S. Abel is an adjunct professor at the Center for Computer Research in Music and Acoustics (CCRMA) in the Music Department at Stanford University, where his research interests include audio and music applications of signal and array processing, parameter estimation, and acoustics. From 1999 to 2007, Abel was a co-founder and chief technology officer of the Grammy Award–winning Universal Audio, Inc. He was a researcher at NASA/Ames Research Center, exploring topics in room acoustics and spatial hearing with a grant from the San Jose State University Foundation. Abel was also chief scientist of Crystal River Engineering, Inc., where he developed their positional audio technology, and a lecturer in the Department of Electrical Engineering at Yale University. As an industry consultant, Abel has worked with Apple, FDNY, LSI Logic, NRL, SAIC, and Sennheiser on projects in professional audio, GPS, medical imaging, passive sonar, and fire department resources allocation. He holds Ph.D. and M.S. degrees from Stanford University, and an S.B. from Massachusetts Institute of Technology, all of which are in electrical engineering. Abel is a Fellow of the Audio Engineering Society.

•

David Berners is Chief Scientist at Universal Audio Inc., a hardware and software manufacturer for the professional audio market. He is also an adjunct professor at the Center for Computer Research in Music and Acoustics (CCRMA) at Stanford University, where he teaches graduate classes in audio effects processing and digital signal processing. Dr. Berners has held positions at the Lawrence Berkeley National Laboratory, NASA Jet Propulsion Laboratory, and Allied Signal. He received his Ph.D. from Stanford University, M.S. from the California Institute of Technology, and his S.B. from Massachusetts Institute of Technology, all in Electrical Engineering.